magnetochemistry

MDPI

Article

Preparation of Activated Carbon-Supported Iron Oxide Composite as a Supercapacitor Electrode Material

Mehmet Firat Baran [1,*], Vedat Tümen [2], Serdar Ekinci [2], Mizgin Özaydin [3], Aziz Eftekhari [4], Abdulkadir Levent [5], Fevzi Yaşar [6], Taras Kavetskyy [7,8,9,*], Ondrej Šauša [9,10], Evgeny Katz [11], Bożena Zgardzińska [12], Davut Izci [13], Rovshan Khalilov [14] and Oleh Smutok [11,*]

[1] Department of Food Technology, Vocational School of Technical Sciences, Batman University, 72000 Batman, Turkey
[2] Department of Computer Engineering, Bitlis Eren University, 13100 Bitlis, Turkey; vtumen@beu.edu.tr (V.T.); sekinci@beu.edu.tr (S.E.)
[3] Batman Provincial Directorate of National Education, Ministry of National Education, 72000 Batman, Turkey; mizgint@gmail.com
[4] Department of Biochemistry, Faculty of Science, Ege University, 35040 İzmir, Turkey; aziz.eftekharimehrabad@ege.edu.tr
[5] Department of Chemistry, Faculty of Arts and Sciences, Batman University, 72100 Batman, Turkey; levent.kadir@batman.edu.tr
[6] Department of Chemistry and Chemical Process Technology, Vocational School of Technical Sciences, Batman University, 72100 Batman, Turkey; fevzi.yasar@batman.edu.tr
[7] Department of Physics and Information Systems, Drohobych Ivan Franko State Pedagogical University, 82100 Drohobych, Ukraine
[8] Department of Biology and Chemistry, Drohobych Ivan Franko State Pedagogical University, 82100 Drohobych, Ukraine
[9] Institute of Physics, Slovak Academy of Sciences, 84511 Bratislava, Slovakia; ondrej.sausa@savba.sk
[10] Department of Nuclear Chemistry, Faculty of Natural Sciences, Comenius University, 84215 Bratislava, Slovakia
[11] Department of Chemistry and Biochemistry, Clarkson University, Potsdam, NY 13699, USA; ekatz@clarkson.edu
[12] Institute of Physics, Maria Curie-Sklodowska University, 20-031 Lublin, Poland; bozena.zgardzinska@mail.umcs.pl
[13] Department of Electrical and Electronics Engineering, Bursa Uludag University, 16059 Bursa, Turkey; davutizci@uludag.edu.tr
[14] Department of Biophysics and Biochemistry, Baku State University, AZ1148 Baku, Azerbaijan; hrovshan@bsu.edu.az
* Correspondence: mehmetfirat.baran@batman.edu.tr (M.F.B.); kavetskyy@yahoo.com (T.K.); osmutok@clarkson.edu (O.S.)

Abstract

The growing demand for sustainable and high-performance energy storage systems has stimulated the development of biomass-derived electrode materials for supercapacitors. In this study, activated carbon (Cm-AC) was synthesized from *Crataegus monogyna* seeds and combined with magnetic iron oxide (Fe_3O_4) nanoparticles to fabricate a hybrid Cm-AC@Fe_3O_4 electrode. The incorporation of iron oxide into the activated carbon matrix altered the charge-storage mechanism from predominantly electrical double-layer capacitance to a hybrid process with a significant faradaic (diffusion-controlled) contribution. Electrochemical measurements in 1 M Na_2SO_4 showed that the specific capacitance increased from 145.92 to 270.68 F g^{-1} at a scan rate of 5 mV s^{-1}. Dunn kinetic analysis revealed that diffusion-controlled faradaic processes accounted for up to 87.82% of the total capacitance at low scan rates, consistent with a dominant contribution from reversible Fe^{2+}/Fe^{3+} redox reactions. Galvanostatic charge–discharge analysis yielded a specific capacitance of 351.51 F g^{-1} at 0.5 A g^{-1}, while electrochemical impedance spectroscopy demonstrated reduced internal and charge-transfer resistances after Fe_3O_4 incorporation. A symmetric Cm-AC@Fe_3O_4 supercapacitor retained 87.5% of its initial capacitance after 10,000 charge–discharge cycles and delivered a maximum energy density of 10.35 Wh kg^{-1} at a power density of

Check for updates

Academic Editor: Roberto Zivieri

Received: 13 August 2026
Revised: 21 September 2026
Accepted: 22 September 2026
Published: 1 October 2026

Copyright: © 2026 by the authors. Licensee MDPI, Basel, Switzerland. This article is an open access article distributed under the terms and conditions of the Creative Commons Attribution (CC BY) license.

396 W kg^{-1}. These findings demonstrate that biomass-derived Cm-AC@Fe_3O_4 is a promising and sustainable electrode material for high-performance supercapacitor applications.

Keywords: activated carbon; *Crataegus monogyna*; Fe_3O_4 nanoparticles; magnetic carbon composite; biomass-derived electrode; supercapacitor; pseudocapacitance; electrochemical energy storage

1. Introduction

Recently, the adverse environmental impact of greenhouse gas emissions has drawn increasing attention to global energy challenges, including the rapid depletion of fossil fuel reserves, rising energy costs, environmental pollution, and CO_2 emissions. According to the International Energy Agency (IEA), global energy-related CO_2 emissions reached a record high of 37.8 Gt in 2024, underscoring the urgency of transitioning to cleaner and more sustainable energy systems [1]. These challenges have created an urgent need to develop efficient, clean, and sustainable energy storage technologies capable of supporting renewable energy conversion while reducing global CO_2 emissions [2]. Supercapacitors, also known as electrochemical capacitors, have emerged as promising energy storage devices because of their high-power density, rapid charge–discharge capability, and long cycle life, and they are widely employed in a variety of electronic and energy storage applications [3–8]. These capacitors offer several advantages, including high specific capacitance, a wide operating temperature range, long cycle life, simple charging and discharging circuitry, fast charging, and low cost [3–8]. Consequently, the development of high-performance electrode materials has become a major focus in supercapacitor research [9]. The performance of supercapacitors is governed by their electrode materials, current collectors, separators, and electrolytes. Among these components, the physicochemical and electrical properties of the electrode material play a decisive role in determining the energy storage performance. Therefore, considerable research efforts have been devoted to developing novel electrode materials with enhanced electrochemical properties [10]. Based on their charge-storage mechanism, supercapacitors can be divided into three categories: electrical double-layer capacitors (EDLCs), pseudocapacitors, and hybrid capacitors [3,11]. In EDLCs, capacitance is directly proportional to the surface area of the electrodes, where energy is stored through electrostatic charge accumulation at the electrode/electrolyte interface [12]. In contrast, pseudocapacitors store energy through rapid and reversible faradaic redox reactions occurring at the electrode/electrolyte interface, resulting in higher specific capacitance than EDLCs [13,14]. Hybrid supercapacitors, which integrate both capacitive and battery-type or pseudocapacitive charge-storage mechanisms, can be broadly classified into two main categories [3]. The first category comprises asymmetric hybrid supercapacitors, which utilize two different electrode materials—typically a capacitive electrode paired with a battery-type or pseudocapacitive electrode—to extend the operating voltage window and enhance energy density [15]. The second category includes metal-ion hybrid capacitors, which combine a battery-type electrode with a capacitor-type electrode and are named according to the working ion, such as lithium-ion, sodium-ion, or zinc-ion hybrid capacitors [4,16].

The charge-storage behavior of supercapacitors is therefore governed by either electrostatic ion adsorption (EDLC mechanism), faradaic redox reactions (pseudocapacitive mechanism), or a combination of both. Carbon-based materials, including carbon nanotubes, carbon nanofibers, carbon aerogels, graphene, and activated carbon, are widely used as EDLC electrode materials because of their high specific surface area, excellent electrical conductivity, and chemical stability. By contrast, pseudocapacitive materials store charge through rapid and reversible faradaic reactions on the electrode surface and commonly in-

clude conductive polymers and transition metal oxides, such as ruthenium dioxide (RuO_2), manganese dioxide (MnO_2), copper oxide (CuO), zinc oxide (ZnO), nickel oxide (NiO), cobalt oxide (Co_3O_4), vanadium oxides (V_2O_5), and iron oxides (Fe_2O_3, Fe_3O_4) [7,8,17–19].

Activated carbon (AC) is one of the most widely used electrode materials for supercapacitors because of its high surface area, good electrical conductivity, and low cost. Despite its excellent power density, AC generally exhibits relatively low specific capacitance, which limits its practical application in high-energy-density devices.

Among transition metal oxides, magnetite (Fe_3O_4) has emerged as a particularly attractive candidate for supercapacitor applications due to its unique combination of physicochemical properties. Fe_3O_4 crystallizes in an inverse spinel structure with the general formula $Fe^{3+}[Fe^{2+}Fe^{3+}]O_4$, where electron hopping between Fe^{2+} and Fe^{3+} ions in the octahedral sites endows it with high electrical conductivity (~10^2 S cm^{-1}) at room temperature—significantly higher than that of other iron oxides such as α-Fe_2O_3 (~10^{-14} S cm^{-1}) [19,20]. Additionally, Fe_3O_4 nanoparticles exhibit intrinsic ferrimagnetic behavior, which can transition to superparamagnetism when the particle size is reduced below a critical threshold (~20–30 nm), enabling magnetic recoverability and potential for magnetically assisted applications [20,21]. From an electrochemical perspective, Fe_3O_4 stores charge through rapid and reversible faradaic redox reactions involving the Fe^{2+}/Fe^{3+} couple, which occur both at the electrode surface and in the near-surface region, contributing to its high theoretical specific capacitance (~2290 F g^{-1} for the three-electron transfer) [19,22]. However, the practical application of pristine Fe_3O_4 as a supercapacitor electrode is hindered by several limitations, including poor cycling stability due to volume changes during repeated redox reactions, particle aggregation, and limited accessibility of active sites [16,23]. To overcome these challenges, various synthesis strategies have been explored, including coprecipitation, hydrothermal, sol–gel, and extraction-pyrolytic methods [24,25], with a particular focus on integrating Fe_3O_4 nanoparticles with conductive carbon matrices to enhance electron transport and structural integrity [16,22,26]. The combination of Fe_3O_4 with activated carbon not only improves electrochemical performance but also offers additional functionality through the magnetic properties of Fe_3O_4, enabling applications such as magnetic separation and magnetically assisted energy storage [21,27].

Iron oxides (Fe_2O_3 and Fe_3O_4) have attracted considerable attention for supercapacitor applications owing to their multiple oxidation states, high theoretical specific capacitance, electrochemical stability, and low cost [8,18,28]. Beyond their electrochemical activity, Fe_3O_4 nanoparticles exhibit intrinsic magnetic properties arising from their spinel ferrite structure, which can exhibit superparamagnetic or ferrimagnetic behavior depending on particle size and morphology. This magnetic character offers additional functionality, such as magnetic recoverability of the electrode material, magnetically assisted ion transport, and potential for magnetically controlled energy storage systems [28,29]. However, both pure Fe_3O_4 and activated carbon exhibit limitations when used individually, including poor electrical conductivity in Fe_3O_4 and limited capacitance in activated carbon. Therefore, integrating Fe_3O_4 nanoparticles with activated carbon to form Cm-AC@Fe_3O_4 hybrid materials represents a promising strategy for enhancing electrochemical performance [29]. Although numerous activated carbon/Fe_3O_4 composites have been reported, little attention has been devoted to activated carbon derived from *Crataegus monogyna* seeds. Recent studies have demonstrated that *C. monogyna* is a promising biomass precursor for activated carbon production. For instance, Ertaş et al. [30] successfully produced magnetic activated carbon from *C. monogyna* for antimicrobial and antioxidant applications, while Baran and Ertaş [31] and Baran et al. [32] utilized *C. monogyna*-based activated carbon nanocomposites for biomedical purposes. Furthermore, the lignocellulosic composition of *C. monogyna* has been characterized, revealing significant cellulose (11.89–13.21%) and lignin (7.71–14.87%)

contents [33–35], which are essential precursors for developing porous carbon structures with tunable surface chemistry. Despite these promising reports, the electrochemical performance of *C. monogyna*-derived activated carbon as a supercapacitor electrode material has not been systematically investigated. Moreover, the influence of Fe_3O_4 incorporation on the charge-storage properties of this specific biomass-derived carbon matrix remains unexplored. The unique lignocellulosic composition and natural mineral content of this biomass may influence pore development, surface chemistry, and the interaction with Fe_3O_4 nanoparticles. Therefore, while Fe_3O_4/biomass-carbon hybridization is a widely explored strategy [8], the genuinely new contribution of this work is threefold: (i) the first electrochemical evaluation of *C. monogyna*-derived activated carbon integrated with Fe_3O_4 nanoparticles; (ii) a quantitative kinetic analysis using Dunn's method to separate capacitive and diffusion-controlled contributions; and (iii) the fabrication and testing of a symmetric supercapacitor device based on this hybrid material. This study aims to evaluate whether this sustainable precursor can provide enhanced electrochemical performance while maintaining a simple and scalable synthesis route.

In this study, a Cm-AC@Fe_3O_4 nanocomposite was synthesized by incorporating magnetic Fe_3O_4 nanoparticles into activated carbon derived from *Crataegus monogyna* (Cm) biomass. This work provides the first systematic electrochemical evaluation of *C. monogyna*-derived activated carbon integrated with Fe_3O_4, including quantitative kinetic analysis via Dunn's method and the fabrication of a symmetric supercapacitor device. The electrochemical performance of the resulting electrode material was systematically evaluated using cyclic voltammetry, galvanostatic charge–discharge measurements, and electrochemical impedance spectroscopy. While the present study focuses primarily on the electrochemical properties, the magnetic nature of Fe_3O_4 opens up possibilities for future exploration of magnetically enhanced charge-storage mechanisms, which remain beyond the scope of this work. The results demonstrate that the Cm-AC@Fe_3O_4 hybrid electrode exhibits enhanced specific capacitance, excellent electrochemical stability, and promising energy-storage characteristics, highlighting its potential for sustainable supercapacitor applications.

2. Materials and Methods

2.1. Chemicals and Reagents

Iron (III) chloride hexahydrate, iron (II) chloride tetrahydrate, hydrochloric acid, sodium hydroxide, ammonium hydroxide, and zinc chloride (all of analytical grade) were purchased from Sigma-Aldrich (Saint Louis, MO, USA). Deionized (DI) water was used throughout the study for material synthesis, solution preparation, and all other experimental procedures.

2.2. Characterization of Materials

The Cm-AC and Cm-AC@Fe_3O_4 nanocomposites were characterized using Fourier transform infrared spectroscopy (FTIR) (Agilent Cary 630 FTIR spectrometer, Agilent Technologies, Santa Clara, CA, USA), scanning electron microscopy (SEM) (LEO EVO 40, LEO Electron Microscopy Ltd., Cambridge, UK), and energy-dispersive X-ray spectroscopy (EDX) (Bruker, 125 eV, Bruker Nano GmbH, Berlin, Germany). The crystal structure of the samples was characterized using a Rigaku D/MAX-2200 X-ray diffractometer (Rigaku Corporation, Tokyo, Japan) and a surface area and porosity analyzer (BET, Micromeritics Instrument Corporation, Norcross, GA, USA).

2.3. Synthesis of Cm-AC from Plant Seeds

To remove impurities from the surface of *Crataegus monogyna* seeds, the seeds were first washed several times with tap water and subsequently rinsed three to four times with

deionized water. After washing, the seeds were dried at room temperature for several days in a dust-free laboratory environment. The dried *C. monogyna* seeds were then ground into a fine powder using an IKA M20 universal blade grinder and stored in a sealed container in the dark until use.

Five grams of the powdered sample was weighed and placed in a 250 mL Erlenmeyer flask. Subsequently, 125 mL of 30% $ZnCl_2$ solution was added, and the mixture was stirred in a shaking water bath at 90 °C for 120 min. After activation, the mixture was cooled to room temperature. The solid product was collected by filtration, transferred to a Petri dish, and dried overnight in an oven at 100 °C. The dried material was placed in a ceramic crucible and carbonized in a muffle furnace at 500 °C. The resulting Cm-AC was cooled to room temperature in a desiccator.

The obtained Cm-AC was washed four to five times with 0.1 M hydrochloric acid (HCl) to remove residual zinc and chlorine species from its surface. Subsequently, the product was washed with deionized water until a neutral pH was reached and dried in an oven at 75 °C for 24 h [21,30,31]. After drying, the Cm-AC was ground, sieved, and stored in an amber bottle for subsequent experimental use.

2.4. Synthesis of Cm-AC@Fe_3O_4 Nanocomposite from Plant Seeds

The surface modification of Cm-AC with magnetic iron oxide (Fe_3O_4) nanoparticles was performed with slight modifications according to previously reported procedures [8,32]. Briefly, 8.0 g of $FeCl_3 \cdot 6H_2O$ was dissolved in 75 mL of ultrapure water. To stabilize the iron ions in solution, 400 µL of concentrated hydrochloric acid was added dropwise under continuous magnetic stirring at room temperature. Subsequently, 3 g of $FeCl_2 \cdot 4H_2O$ was added to the Fe^{3+}-containing solution.

The reaction mixture was gradually heated to 90 °C and stirred continuously for 30 min. Thereafter, 15 mL of 28% ammonium hydroxide solution was added dropwise to the mixture containing iron (III) and iron (II) ions. Following the formation of the black Fe_3O_4 precipitate, the mixture was stirred at 90 °C for an additional 30 min.

Next, a suspension containing 500 mg of Cm-AC in 75 mL of deionized water was slowly added to the reaction mixture. After 1 h of stirring at 90 °C, heating was discontinued, and the synthesized Cm-AC@Fe_3O_4 nanocomposite was allowed to cool naturally to 25 °C. The resulting Cm-AC@Fe_3O_4 nanocomposite was separated from the reaction mixture using an external magnet [15].

To remove residual reactants, the Cm-AC@Fe_3O_4 nanocomposite was washed several times with deionized water and subsequently dried in an oven at 75 °C. After drying, the Cm-AC@Fe_3O_4 nanocomposite was stored in an amber container for subsequent electrochemical characterization.

2.5. Electrochemical Measurement Methods and Experimental Conditions

The energy storage performance of the synthesized Cm-AC and Cm-AC@Fe_3O_4 biomass-derived electrode materials was investigated using an AUTOLAB PGSTAT 128N potentiostat/galvanostat system (Metrohm Autolab, Utrecht, The Netherlands). Electrochemical characterization studies were performed using three-electrode and two-electrode configurations to evaluate both the fundamental electrochemical properties of the materials and their performance in practical supercapacitor devices. Cyclic voltammetry (CV), galvanostatic charge–discharge (GCD), and electrochemical impedance spectroscopy (EIS) techniques were employed to evaluate the charge-storage behavior, electrode kinetics, and ion transport properties of the samples. CV measurements were used to analyze the redox activity and capacitive response of the electrode materials, whereas GCD measurements were performed to determine the specific capacitance, energy density, and power density

values. EIS analyses were conducted to investigate the charge-transfer resistance at the electrode/electrolyte interface, ion diffusion behavior, and overall internal resistance of the electrochemical system.

EIS measurements were performed at open-circuit potential (OCP) after the supercapacitor cells were fully discharged by applying an alternating current (AC) perturbation with a frequency range of 100 kHz–0.01 Hz and an amplitude of 10 mV. All electrochemical experiments were carried out in a 1 M Na_2SO_4 electrolyte solution to ensure high ionic conductivity.

2.6. Electrode Configuration and Electrode Preparation Procedure

For measurements performed using a three-electrode system, platinum (Pt) wire was used as the counter (auxiliary) electrode, while an Ag/AgCl (3 M KCl) electrode served as the reference electrode. In two-electrode measurements, conducted to evaluate the practical device performance of the electrode materials, a symmetric supercapacitor configuration was employed.

The carbon paste electrode (CPE) method was used for the preparation of supercapacitor electrodes. The active electrode material (Cm-AC or Cm-AC@Fe_3O_4), conductive graphite, and mineral oil as a binder were combined in a ratio of 75%:5%:20% (mass ratio), respectively [10]. The components were mechanically mixed until a homogeneous paste was obtained. The prepared composite paste was introduced into the cavity of the carbon paste electrode body and manually compressed to obtain a uniform electrode surface, minimize contact resistance, and improve electrochemical performance. The prepared electrodes were used directly for electrochemical measurements.

The specific capacitance (Csp) of the prepared electrodes was evaluated using CV, GCD, and EIS measurements in an aqueous 1 M Na_2SO_4 electrolyte. The capacitance values were calculated using established electrochemical equations corresponding to each characterization technique.

For CV analysis, the specific capacitance was calculated from the integrated area of the voltammogram according to the following equation:

$$C_{sp} = \frac{A}{2r\Delta Vm}$$

where A is the integrated area of the CV curve, r represents the scan rate, ΔV denotes the applied potential window, and m corresponds to the mass of the electroactive material.

For GCD measurements performed in a three-electrode configuration, the specific capacitance was calculated using:

$$C_{sp} = \frac{It_d}{\Delta Vm}$$

For the symmetric two-electrode GCD configuration, the capacitance calculation was modified to account for the contribution of both electrodes:

$$C_{sp} = \frac{It_d}{2\Delta Vm}$$

where I is the applied discharge current and t_d represents the discharge time. The capacitance values obtained from GCD curves were calculated only from the linear discharge region, while the initial IR drop was excluded. This approach minimizes the influence of ohmic resistance and internal voltage losses, providing a more accurate evaluation of the intrinsic charge-storage capability of the electrode materials.

For EIS measurements, the specific capacitance was estimated from the imaginary component of impedance at the corresponding frequency according to:

$$C_{sp} = \frac{1}{2\pi f \mid Z'' \mid m}$$

where f is the applied frequency and |Z″| represents the imaginary component of impedance.

In addition to capacitance evaluation, the energy density (E_d) and power density (P_d) of the electrochemical system were calculated to assess practical device performance. The energy density (Wh kg^{-1}) was determined using:

$$E_d = \frac{C_{sp}(\Delta V)^2}{2 \times 3.6}$$

The corresponding power density (W kg^{-1}) was calculated as:

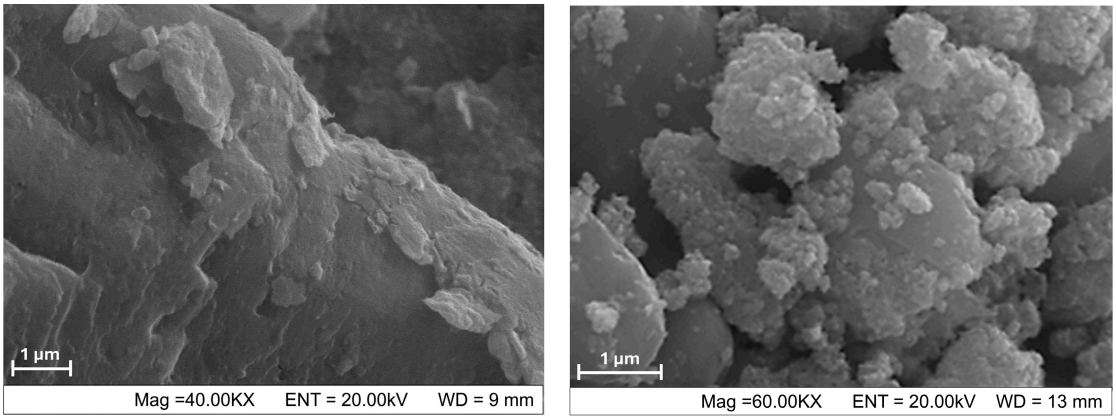
$$P_d = \frac{E_d}{t_d} \times 3600$$

All reported capacitance, energy density, and power density values were normalized with respect to the active mass of the electrode material to ensure consistency and comparability. The use of identical electrolyte conditions throughout the measurements enabled reliable comparison of electrochemical performance under different testing configurations.

3. Results and Discussion

3.1. SEM Analysis of Cm-AC and Cm-AC@Fe_3O_4 Biomass-Derived Nanomaterials

The morphological characteristics of Cm-AC and Cm-AC@Fe_3O_4 biomass-derived nanocomposites were investigated using scanning electron microscopy (SEM). The SEM images presented in Figure 1a,b illustrate the surface morphology of Cm-AC and Cm-AC@Fe_3O_4, respectively.



(**a**) (**b**)

Figure 1. SEM images of (**a**) Cm-AC and (**b**) Cm-AC@Fe_3O_4 biomass-derived nanocomposites.

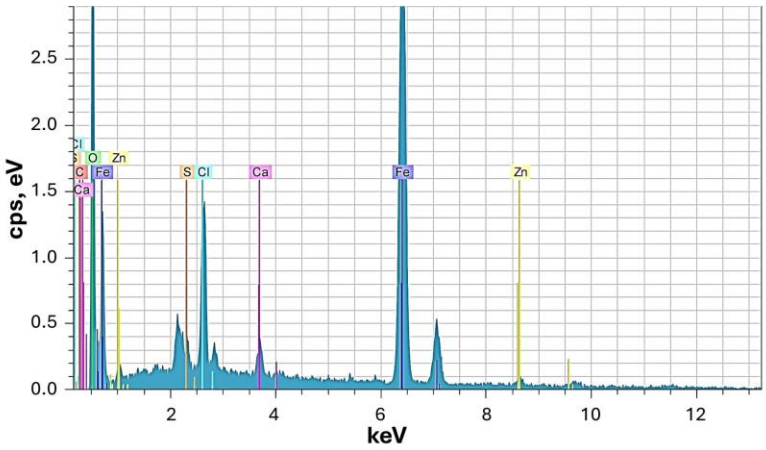
The morphology of Cm-AC reveals aggregated carbon particles with a clustered structure (Figure 1a). Such aggregation may reduce the accessible surface area and hinder efficient electron transport within the electrode material.

Figure 1b shows the morphology of the Cm-AC@Fe_3O_4 hybrid nanocomposite, revealing a more uniform distribution of Fe_3O_4 nanoparticles throughout the activated carbon matrix and reduced particle aggregation after composite formation. The improved dispersion of Fe_3O_4 nanoparticles is expected to provide additional electroactive sites and facilitate ion diffusion at the electrode/electrolyte interface, contributing to enhanced electrochemical performance [36].

3.2. EDX Analysis of Cm-AC@Fe_3O_4 Biomass-Derived Nanomaterials

Energy-dispersive X-ray spectroscopy (EDX) is a widely used technique for evaluating the elemental composition and chemical purity of synthesized materials. The EDX spectrum

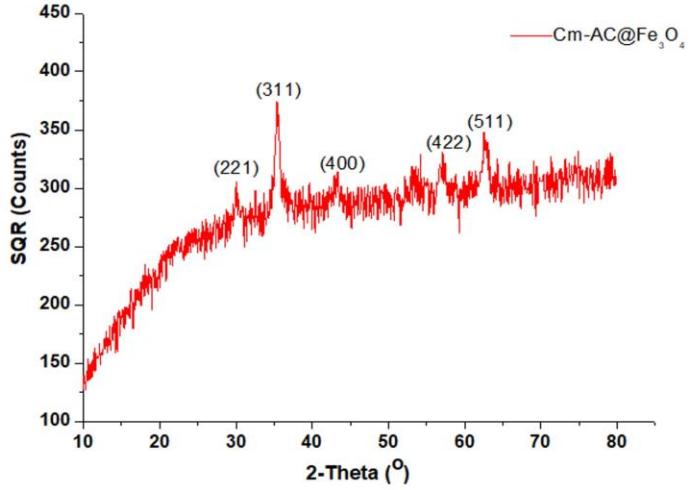
of the Cm-AC@Fe_3O_4 nanocomposite (Figure 2) confirms the presence of Fe, O, and C elements, indicating the successful incorporation of magnetic iron oxide into the activated carbon matrix.



(a)

Element	Unn. C (wt.%)	Norm. C (wt.%)	Atomic C (at.%)	Error (%)
Fe	52.71	59.13	34.17	1.5
Cl	5.28	5.92	5.39	0.2
Zn	4.10	4.59	2.27	0.2
S	1.63	1.83	1.84	0.1
Ca	1.20	1.34	1.08	0.1
C	0.55	0.62	1.66	0.3
O	23.68	26.56	53.58	3.4
Total	89.14	100.00	100.00	—

(b)



(c)

Figure 2. EDX spectrum (**a**) and elemental composition (**b**), and crystal structure via X-ray diffraction (XRD) (**c**) of the Cm-AC@Fe_3O_4 biomass-derived nanocomposite.

The high content of Fe and O is associated with the formation of Fe_3O_4 nanoparticles, whereas carbon originates from the biomass-derived activated carbon framework. The additional elements detected, including Cl, Zn, S, and Ca, are likely associated with residual impurities originating from the chemical activation process and biomass precursors.

The XRD pattern of the synthesized material (Figure 2c) exhibited characteristic diffraction peaks at 2θ values corresponding to the (220), (311), (400), (422), and (511) crystallographic planes of magnetite (Fe_3O_4). These reflections are in good agreement with the standard JCPDS card No. 01-071-6336, confirming the formation of single-phase, highly crystalline cubic spinel Fe_3O_4 with the space group Fd-3m. Among these reflections, the (311) plane exhibited the highest intensity, which is characteristic of magnetite nanoparticles and may indicate a preferential crystallographic orientation along this plane [36,37].

3.3. BET Surface Area Analysis of Cm-AC and Cm-AC@Fe_3O_4 Biomass-Derived Nanocomposites

The specific surface areas of Cm-AC and Cm-AC@Fe_3O_4 biomass-derived nanocomposites were evaluated using Brunauer–Emmett–Teller (BET) analysis (adsorption–desorption isotherms), as shown in Figure 3.

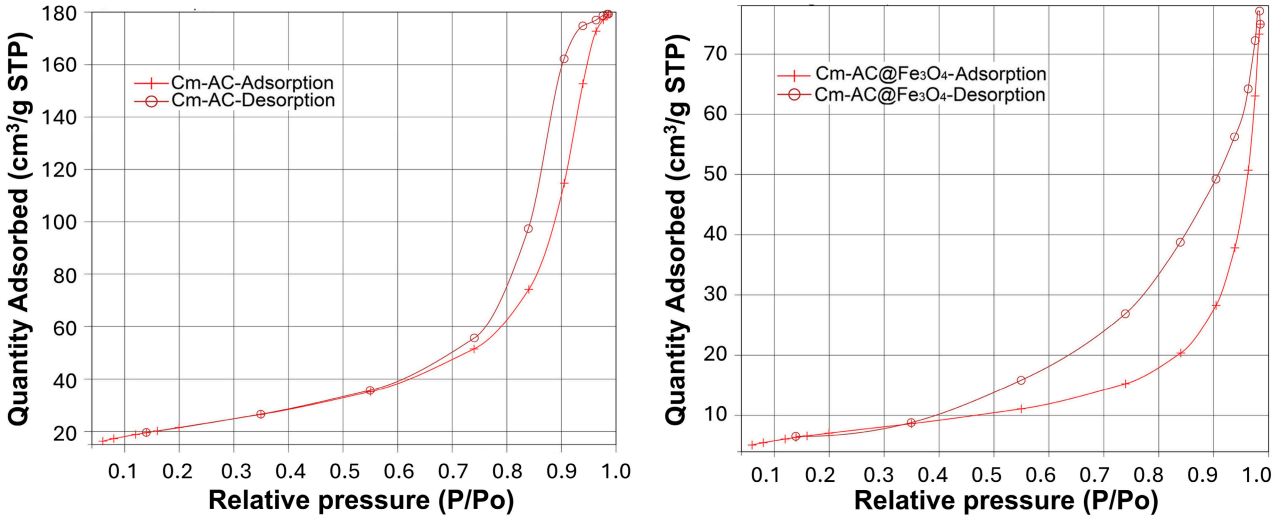


Figure 3. BET adsorption–desorption isotherms of (**a**) Cm-AC and (**b**) Cm-AC@Fe_3O_4 biomass-derived nanocomposites.

In the N_2 adsorption–desorption isotherms of the Cm-AC and Cm-AC@Fe_3O_4 samples, a distinct hysteresis in the medium-to-high relative pressure range and a significant increase in the amount of adsorbed N_2 at high (P/P_0) values were observed. According to the IUPAC classification, these characteristics are more consistent with Type IV physisorption behavior than with Type III behavior. Type IV isotherms are characteristic of mesoporous systems and are associated with capillary condensation within mesopores [38]. The BET surface areas of Cm-AC and Cm-AC@Fe_3O_4 were calculated to be 72.26 and 24.97 $m^2\ g^{-1}$, respectively. The substantial decrease in surface area after Fe_3O_4 incorporation is attributed to the partial occupation or blockage of carbon pores by Fe_3O_4 nanoparticles, which reduces the accessible porosity. This reduction is a direct consequence of nanoparticle deposition within the carbon matrix.

Although this pore blocking effect significantly lowers the specific surface area, the electrochemical performance of the hybrid electrode improves considerably (as discussed in Sections 3.5–3.7). This apparent contradiction is resolved by recognizing that the capacitance enhancement originates primarily from the faradaic redox activity of Fe_3O_4 nanoparticles, which introduce additional electrochemically active sites that compensate for the lost physical surface area. In other words, the increase in capacitance is not due to improved physical ion accessibility, but rather to the chemical charge-storage contribution from the Fe^{2+}/Fe^{3+} redox couple. The carbon matrix, despite the reduced porosity, still acts as a conductive scaffold that facilitates electron transfer to these redox centers, as evidenced by the decreased charge-transfer resistance observed in EIS analysis. Thus, the hybrid material benefits from a complementary mechanism: the carbon provides electrical conductivity and some EDLC contribution, while Fe_3O_4 supplies faradaic charge-storage, even though the overall porosity is reduced. Although pore-size distribution and micropore/mesopore volume analyses were not performed in this study, the Type IV isotherm confirms the mesoporous nature of both materials, and the combined BET–EIS data consistently support the interpretation that the performance enhancement is governed by faradaic contributions rather than improved physical ion diffusion.

3.4. FTIR Analysis of Cm-AC Biomass-Derived Nanocomposite

Figure 4 presents the FTIR spectrum of Cm-AC and illustrates the characteristic functional groups present on the activated carbon surface. The broad absorption band at

3343 cm^{-1} corresponds to the stretching vibration of hydroxyl (–OH) groups, while the peak at 2922 cm^{-1} is attributed to aliphatic C–H stretching vibrations.

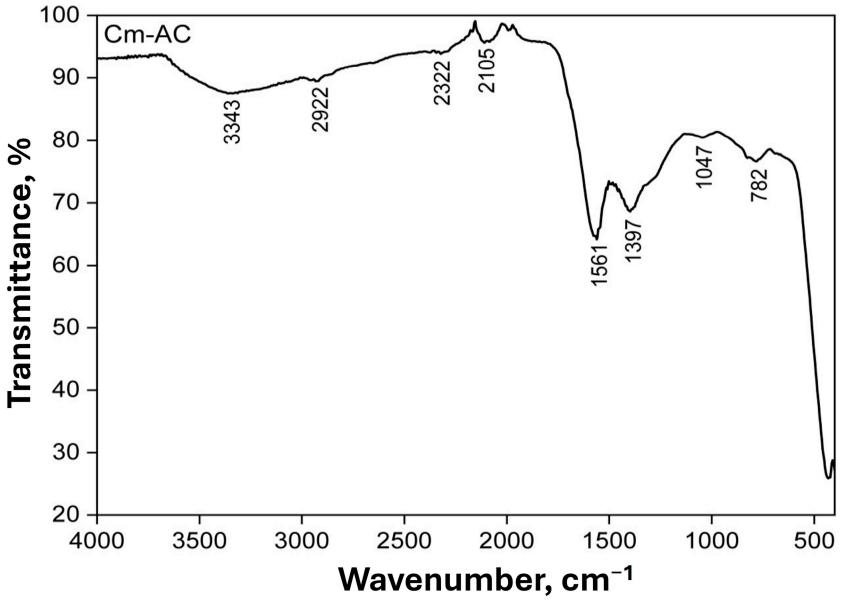


Figure 4. FTIR spectrum of Cm-AC biomass-derived activated carbon.

The absorption band observed at 2105 cm^{-1} corresponds to the C≡C stretching vibration of alkyne groups. The peak at 1561 cm^{-1} is assigned to C=C stretching vibrations of aromatic structures, while the band at 1397 cm^{-1} corresponds to C–H bending vibrations of methyl groups. The peaks located at 1047 cm^{-1} and 782 cm^{-1} are attributed to C–O stretching vibrations and aromatic C–H bending vibrations, respectively.

The presence of oxygen-containing functional groups confirms the successful formation of biomass-derived activated carbon and indicates the availability of surface functional groups that may contribute to electrolyte interaction and electrochemical activity.

3.5. Electrochemical Performance Analysis: Cyclic Voltammetry

The energy storage behavior of Cm-AC and Cm-AC@Fe_3O_4 biomass-derived electrode materials prepared from *Crataegus monogyna* seeds was investigated using cyclic voltammetry (CV) in a 1 M Na_2SO_4 electrolyte within a potential window of 0.0–1.1 V. This potential range was selected based on the stability window of the neutral aqueous electrolyte (~1.23 V theoretical limit, with practical operation typically restricted to ~1.0–1.1 V to avoid water decomposition) and the stable reversible redox activity of the Fe_3O_4 phase within this region, as confirmed by preliminary experiments. The chosen window is also consistent with literature reports for similar carbon/metal oxide composites in Na_2SO_4 electrolytes [8,16,23]. Figure 5a presents the comparative CV curves obtained at a scan rate of 5 mV s^{-1}, along with the corresponding calculated specific capacitance (Csp) values.

The CV results demonstrated that the pristine Cm-AC biomass-derived activated carbon electrode exhibited a specific capacitance of 145.92 F g^{-1}. One of the most effective strategies reported in the literature to overcome the limited capacitance of carbon-based electrodes is the incorporation of transition metal oxides into carbon matrices [8,16,23,27,39–42]. Accordingly, the Cm-AC@Fe_3O_4 hybrid electrode, obtained through the incorporation of Fe_3O_4 nanoparticles into the Cm-AC framework, exhibited significantly enhanced electrochemical performance. As shown in Figure 5a, the specific capacitance increased from 145.92 F g^{-1} for Cm-AC to 270.68 F g^{-1} for Cm-AC@Fe_3O_4, corresponding to an 85.49% improvement after Fe_3O_4 modification. The simultaneous increase in capacitance despite the

reduction in BET surface area indicates that the electrochemical improvement originates predominantly from faradaic charge-storage rather than increased accessible surface area.

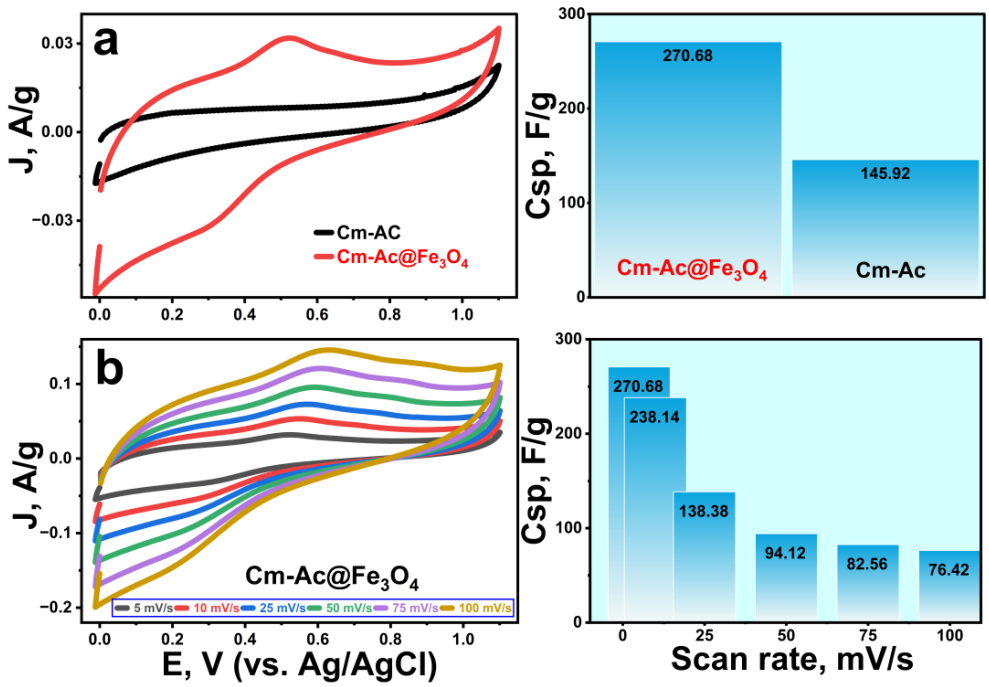


Figure 5. CV analysis of Cm-AC and Cm-AC@Fe_3O_4 electrodes in 1 M Na_2SO_4 electrolyte: (**a**) comparative CV curves and calculated specific capacitance values at a scan rate of 5 mV s^{-1}; (**b**) CV curves and corresponding specific capacitance values of the Cm-AC@Fe_3O_4 electrode at different scan rates (5–100 mV s^{-1}).

The enhanced capacitance can be attributed to the beneficial complementary contributions of the conductive carbon framework and the electroactive Fe_3O_4 phase. Although a direct electrochemical comparison with pure Fe_3O_4 was not within the scope of this study, the substantial increase in capacitance despite the reduced specific surface area (as confirmed by BET analysis) provides strong indirect evidence that the carbon matrix serves as an effective conductive scaffold, enabling the Fe_3O_4 nanoparticles to contribute to the overall charge-storage process through faradaic redox reactions. While charge-storage in the pristine Cm-AC electrode primarily occurs through the electrical double-layer capacitance (EDLC) mechanism involving electrostatic ion adsorption on the porous carbon surface, the incorporation of Fe_3O_4 introduces additional pseudocapacitive charge-storage processes through reversible faradaic reactions. Similar enhancement effects have been reported for carbon/metal oxide hybrid electrode systems [8,16,20,22,23,26,27,43].

The improved electrochemical performance of the Cm-AC@Fe_3O_4 electrode can be attributed to the following factors:

(i) Redox activity: The rapid and reversible Fe^{2+}/Fe^{3+} redox reactions occurring at the electrode/electrolyte interface provide additional faradaic charge-storage sites, thereby increasing the specific capacitance of the hybrid electrode.

(ii) Enhanced ion transport and electrochemical accessibility: The uniform distribution of Fe_3O_4 nanoparticles within the carbon matrix generates additional electroactive sites and facilitates electrolyte ion diffusion, improving the accessibility of internal porous structures.

(iii) Structural and electrochemical stability: The integration of Fe_3O_4 nanoparticles into the activated carbon matrix contributes to improved structural integrity and maintains stable charge-storage behavior over the applied potential range of 0.0–1.1 V.

The electrochemical kinetics of the Cm-AC@Fe_3O_4 hybrid electrode were further investigated by CV measurements at different scan rates ranging from 5 to 100 mV s^{-1} (Figure 5b). The CV curve area increased with increasing scan rate; however, the calculated specific capacitance gradually decreased. The highest capacitance value of 270.68 F g^{-1} was obtained at 5 mV s^{-1}, whereas it decreased to 76.42 F g^{-1} at 100 mV s^{-1}. This decrease is attributed to insufficient ion diffusion time at higher scan rates, which limits access to inner pores and restricts the contribution of faradaic reactions within the electrode structure [23,26,27,42,44].

To quantitatively distinguish the contributions of capacitive (surface-controlled) and diffusion-controlled processes, the Dunn method was applied to the Cm-AC@Fe_3O_4 electrode [45–47]. The current response was analyzed according to the relationship:

$$J(V) = k_1 v + k_2 v^{1/2}$$

where $k_1 v$ represents the capacitive contribution arising from surface-controlled charge-storage (including electric double-layer formation and any fast surface faradaic reactions), and $k_2 v^{1/2}$ corresponds to the diffusion-controlled contribution originating from faradaic reactions that are limited by ionic diffusion. The fitting procedure was performed at representative potentials (0.2, 0.4, 0.6, and 0.8 V vs. Ag/AgCl) across all scan rates (5–100 mV s^{-1}). At each potential, the current response $i(V)$ was plotted against the scan rate v, and the parameters k_1 and k_2 were determined from the slope and intercept of the linear regression of $i(V)/v^{1/2}$ versus $v^{1/2}$, respectively. The linear regression coefficients (R^2) for all fitted potentials ranged from 0.986 to 0.993, indicating excellent goodness of fit and validating the applicability of the Dunn method to our system. At a low scan rate of 5 mV s^{-1}, the capacitive contribution was found to be 12.18%, whereas the diffusion-controlled faradaic contribution was 87.82%. This indicates that at slow scan rates, electrolyte ions have sufficient time to diffuse into the electrode interior and access the Fe_3O_4 active sites, enabling extensive faradaic redox reactions. When the scan rate was increased to 100 mV s^{-1}, the capacitive contribution increased to 38.30%, while the diffusion-controlled contribution decreased to 61.70%. This trend is typical for hybrid electrodes: at high scan rates, charge-storage is dominated by fast surface processes, whereas the diffusion-limited faradaic reactions become less accessible. These results confirm that the Cm-AC@Fe_3O_4 electrode exhibits a hybrid charge-storage mechanism, with diffusion-controlled faradaic processes being the major contributor at low rates, and capacitive processes becoming more significant at high rates. It is important to note that while the diffusion-controlled faradaic contribution is consistent with the reversible Fe^{2+}/Fe^{3+} redox activity of Fe_3O_4 (as evidenced by the well-defined redox peaks in the CV curves at ~0.65 V/0.45 V), direct spectroscopic confirmation of the Fe oxidation states (e.g., via XPS or Mössbauer spectroscopy) was not performed in this study. Therefore, the assignment of the diffusion-controlled contribution specifically to Fe^{2+}/Fe^{3+} redox reactions, while strongly supported by the electrochemical data, remains indirect. Future studies incorporating XPS analysis would be valuable to directly verify the oxidation state changes during charge–discharge cycling.

3.6. Evaluation of Electrochemical Performance Through Galvanostatic Charge–Discharge Analysis

Galvanostatic charge–discharge (GCD) analysis is a fundamental electrochemical technique widely used to quantitatively evaluate the charge-storage capability, specific capacitance, energy-storage efficiency, and charge-transfer behavior of electrode materials under controlled operating conditions. In this study, because the CV results demonstrated superior electrochemical performance of the Cm-AC@Fe_3O_4 hybrid electrode compared with pristine Cm-AC, further GCD measurements were performed only for the Cm-AC@Fe_3O_4 electrode. The GCD experiments were conducted in a 1 M Na_2SO_4 electrolyte solution at current densities ranging from 0.5 to 0.9 A g^{-1} within a potential window of 0.0–1.1 V (versus Ag/AgCl reference electrode).

The GCD profiles presented in Figure 6a exhibit deviations from the ideal symmetric triangular shape characteristic of a purely electrical double-layer capacitor (EDLC). The presence of plateaus and slight deviations from linearity indicates that, in addition to ion adsorption-based EDLC behavior, faradaic redox reactions contribute significantly to the overall charge-storage mechanism [8,16,23]. This behavior is consistent with the redox features observed in the CV curves and supports the conclusion that a significant fraction of the stored charge is associated with reversible Fe^{2+}/Fe^{3+} redox reactions associated with Fe_3O_4 nanoparticles. The relatively symmetric charge–discharge profiles further suggest good reversibility of these diffusion-controlled faradaic processes during repeated charge–discharge cycles under the investigated current densities. Nevertheless, the highly reversible and nearly symmetric nature of the GCD curves suggests that the Cm-AC@Fe_3O_4 hybrid electrode exhibits good electrical conductivity and efficient charge-transfer kinetics. The specific capacitance values summarized in Figure 6b demonstrate the dependence of electrochemical performance on the applied current density. A maximum specific capacitance of 351.51 F g^{-1} was achieved at the lowest current density of 0.5 A g^{-1}, indicating that under slower charge–discharge conditions, electrolyte ions (Na^+ and SO_4^{2-}) have sufficient time to diffuse into the porous structure and access internal electroactive sites of the electrode [48,49].

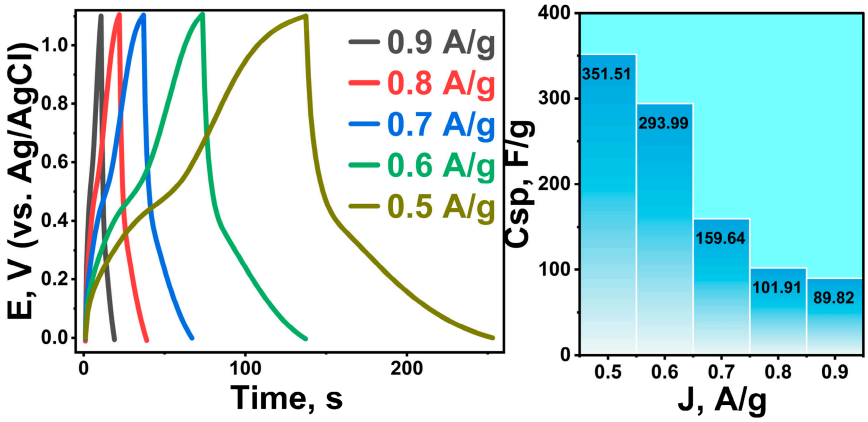


Figure 6. Electrochemical performance of the Cm-AC@Fe_3O_4 hybrid electrode: (**a**) galvanostatic charge–discharge curves at different current densities; (**b**) variation in calculated specific capacitance with current density.

This observation agrees well with the low charge-transfer resistance obtained from EIS analysis and the dominant pseudocapacitive contribution identified by CV/Dunn analysis. When the current density was increased to 0.9 A g^{-1}, the specific capacitance decreased to 89.82 F g^{-1}. This reduction can be attributed to kinetic limitations associated with rapid charge–discharge processes. At higher current densities, electrolyte ions have insufficient time to penetrate smaller pores and access deeper electroactive regions, resulting in charge-storage being mainly restricted to the external surface and larger pores of the electrode [20,23,27,43].

Furthermore, increasing the current density enhances the influence of the internal resistance and ionic transport limitations, leading to a larger IR drop, reduced discharge time, and consequently lower calculated capacitance values. Therefore, although the faradaic reactions of Fe_3O_4 remain active near the electrode surface, the accessibility of internal Fe_3O_4 active sites becomes partially limited under high-rate conditions.

Overall, the GCD results demonstrate that the Cm-AC@Fe_3O_4 hybrid electrode benefits from the combined advantages of the porous carbon framework and the pseudocapacitive

contribution of Fe_3O_4 nanoparticles. These findings confirm that the Cm-AC@Fe_3O_4 composite possesses promising charge-storage characteristics and balanced electrochemical performance for supercapacitor applications.

3.7. Electrochemical Impedance Spectroscopy Analysis

To further investigate the electrochemical kinetics, charge-transfer processes at the electrode/electrolyte interface, and ion diffusion characteristics of the Cm-AC and Cm-AC@Fe_3O_4 electrode materials, electrochemical impedance spectroscopy (EIS) measurements were performed. The measurements were conducted after complete discharge of the electrochemical cells at open-circuit potential (OCP), using an AC perturbation amplitude of 10 mV over a frequency range of 100 kHz to 0.01 Hz. The corresponding Nyquist plots are presented in Figure 7a.

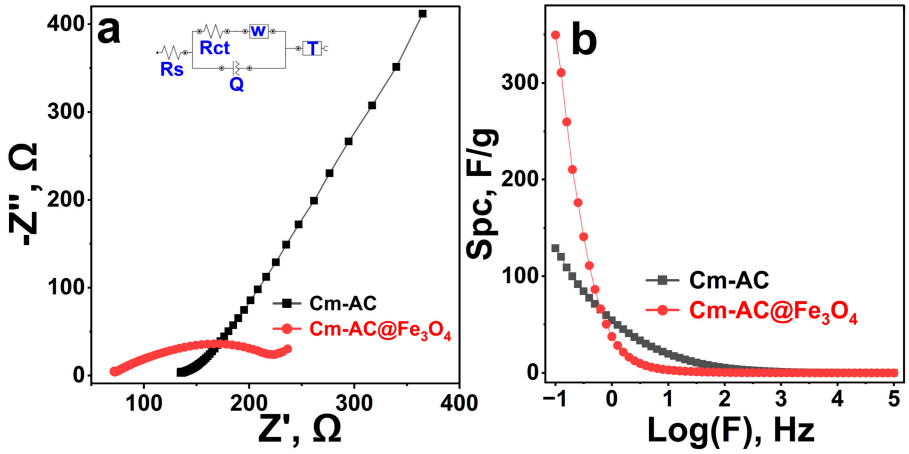


Figure 7. Electrochemical impedance spectroscopy and capacitance comparison of Cm-AC and Cm-AC@Fe_3O_4 electrodes: (**a**) Nyquist plots; (**b**) calculated specific capacitance values.

The intercept of the Nyquist curve with the Z′ axis in the high-frequency region corresponds to the equivalent series resistance (Rs), which includes the electrolyte resistance, electrode intrinsic resistance, and contact resistance between the electrode and current collector. The Rs value of the Cm-AC electrode was determined to be approximately 135 Ω, whereas the Cm-AC@Fe_3O_4 hybrid electrode exhibited a reduced Rs value of approximately 72 Ω. This decrease in *Rs* after Fe_3O_4 incorporation indicates a reduction in the overall series resistance of the electrochemical system, which may be associated with improved electrode conductivity, better interfacial contact, or more efficient ionic pathways within the hybrid structure. The decrease in Rs after Fe_3O_4 incorporation indicates improved electrical conductivity and enhanced ion transport within the hybrid electrode structure [8,16,20,23,27].

The semicircular region in the intermediate-frequency range is associated with the charge-transfer resistance (Rct) arising from faradaic processes at the electrode/electrolyte interface. The diameter of this semicircle reflects the magnitude of Rct. For the Cm-AC electrode, the Rct value was estimated to be approximately 65 Ω, indicating relatively limited faradaic contribution and a charge-storage mechanism primarily governed by EDLC behavior. In contrast, the Cm-AC@Fe_3O_4 electrode exhibited a significantly smaller semicircle with an Rct value of approximately 15 Ω. This reduction demonstrates that Fe_3O_4 nanoparticles provide additional electroactive sites and facilitate rapid reversible Fe^{2+}/Fe^{3+} redox reactions, thereby accelerating charge-transfer kinetics within the hybrid electrode.

The EIS results are consistent with the kinetic analysis obtained from CV measurements using the Dunn method. At a scan rate of 5 mV s^{-1}, 87.82% of the total capacitance of the Cm-AC@Fe_3O_4 electrode was attributed to diffusion-controlled faradaic processes, while

the capacitive contribution accounted for 12.18%. Therefore, the reduced *Rct* value and suppressed semicircle observed in the EIS spectrum provide additional evidence for the enhanced faradaic charge-storage introduced by Fe_3O_4 modification.

In the low-frequency region, the Cm-AC electrode exhibited a less steep linear response, suggesting greater diffusion limitations and a predominantly EDLC-based charge-storage mechanism. In comparison, the Cm-AC@Fe_3O_4 electrode displayed a steeper slope approaching the ideal capacitive behavior, indicating that both faradaic reactions and electrical double-layer charging contribute to the overall hybrid charge-storage mechanism [22,27].

The impedance spectra were fitted using the Rs(Rct||CPE)-W equivalent circuit model [8]. In this model, the constant phase element (CPE, Q) accounts for the non-ideal capacitive behavior associated with surface heterogeneity and porous electrode structures. The fitted parameters obtained from the equivalent circuit analysis were as follows: for the Cm-AC electrode, *R*s = 135.2 ± 2.1 Ω, Rct = 65.3 ± 1.5 Ω, Q = 0.012 ± 0.001 F^{sn-1}, n = 0.88 ± 0.02, and Warburg resistance W = 8.5 ± 0.5 $\Omega^{s-1/2}$, with a goodness-of-fit parameter $\chi^2 = 1.2 \times 10^{-3}$. For the Cm-AC@$Fe_3O_4$ hybrid electrode, the fitted values were Rs = 72.4 ± 1.8 Ω, Rct = 15.2 ± 0.9 Ω, Q = 0.085 ± 0.003 F^{sn-1}, n = 0.78 ± 0.02, W = 3.2 ± 0.3 Ω $s^{-1/2}$, and $\chi^2 = 8.5 \times 10^{-3}$. The low χ^2 values confirm the quality of the fits. The Rs values obtained for both electrodes are relatively high for aqueous electrolyte systems, which can be attributed to several factors: (i) the use of mineral oil binder in electrode fabrication, which introduces additional resistance; (ii) the intrinsic resistance of the biomass-derived activated carbon; and (iii) contact resistance between the electrode and the current collector. Similar Rs values (in the range of 50–150 Ω) have been reported for binder-containing electrodes fabricated from low-cost biomass-derived carbons in aqueous electrolytes. The decrease in Rs after Fe_3O_4 incorporation (from ~135 Ω to ~72 Ω) suggests an improvement in the overall series resistance, which may be associated with enhanced electrode conductivity and/or better interfacial contact. However, we acknowledge that this decrease should not be overinterpreted as direct evidence of "good conductivity" without considering the contributions from other system components.

The higher n value (0.85–0.90) obtained for the Cm-AC electrode indicates a more uniform surface with a stronger EDLC contribution. In contrast, the Cm-AC@Fe_3O_4 electrode exhibited an increased Q value and a reduced n parameter (0.75–0.80), suggesting that Fe_3O_4 nanoparticles increase surface heterogeneity and generate additional electroactive regions, thereby enhancing faradaic charge-storage behavior.

The impedance results are further supported by the capacitance values obtained from electrochemical measurements. As shown in Figure 7b, the specific capacitance calculated for the Cm-AC electrode was 128.34 F g^{-1}, whereas the Cm-AC@Fe_3O_4 hybrid electrode reached 349.62 F g^{-1} using the procedure described in the experimental section (Section 2.6). The approximately threefold enhancement in capacitance is attributed to the combined effects of reduced internal resistance, improved charge-transfer kinetics, and additional faradaic charge-storage provided by Fe_3O_4 nanoparticles.

Overall, the combined EIS, CV, and Dunn kinetic analyses demonstrate that Fe_3O_4 incorporation effectively modifies the charge-storage mechanism of the Cm-AC electrode from an EDLC-dominated system toward a hybrid electrode with a substantial faradaic (diffusion-controlled) contribution. The reduced Rs and Rct values, together with enhanced electrochemical activity, explain the improved capacitance and rate capability of the Cm-AC@Fe_3O_4 hybrid electrode.

3.8. Evaluation of Symmetric Supercapacitor Device Performance: Cyclic Stability and Energy–Power Characteristics

Following the superior electrochemical performance demonstrated by the Cm-AC@Fe_3O_4 hybrid electrode in the three-electrode configuration, a symmetric Cm-AC@Fe_3O_4//Cm-AC@Fe_3O_4 supercapacitor device was assembled to evaluate its practical electrochemical applicability. The assembled device was investigated in terms of long-term cycling stability and the relationship between energy and power density, which are important parameters for evaluating supercapacitor performance.

The ability of an energy storage device to retain its capacitance over extended cycling is a critical factor for practical applications. Therefore, the cycling stability of the symmetric device was evaluated by performing 10,000 consecutive galvanostatic charge–discharge (GCD) cycles at a constant current density of 0.5 A g^{-1} (Figure 8a). After completion of the cycling test, the device retained 87.5% of its initial capacitance. This retention value demonstrates good long-term stability of the Fe_3O_4-containing hybrid electrode system, considering that metal oxide-based electrodes may experience structural stress associated with repeated redox processes and volume changes during cycling [8,16,27,40,43,46].

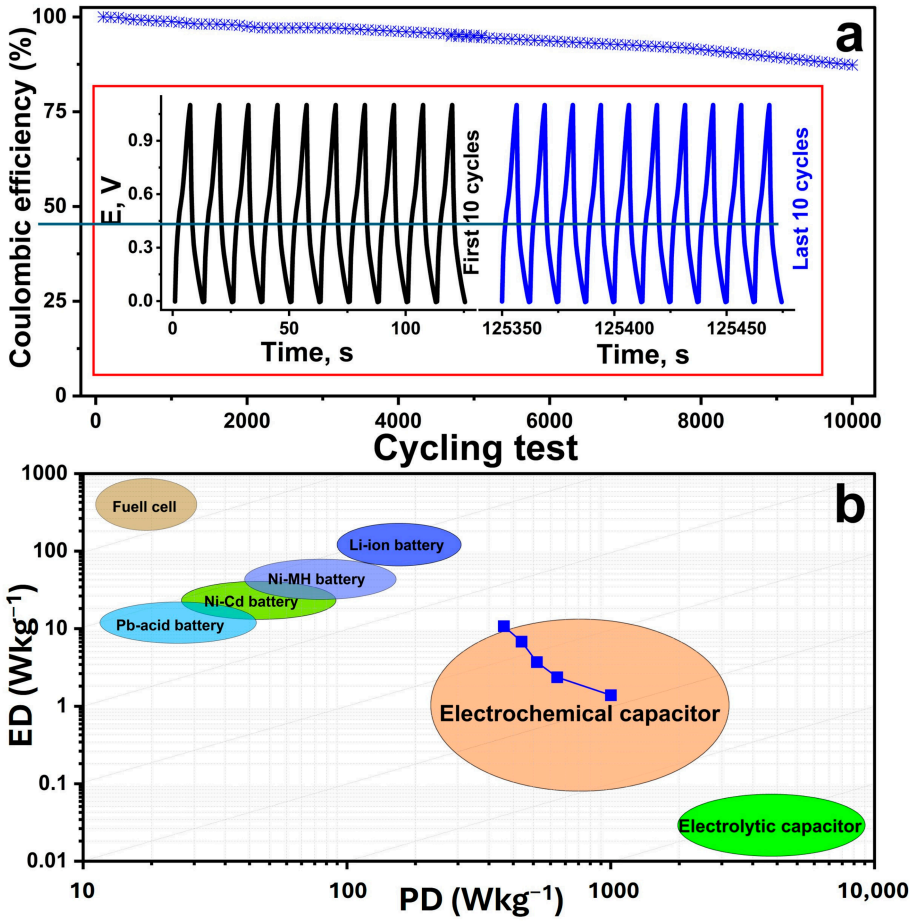


Figure 8. Electrochemical performance of the symmetric Cm-AC@Fe_3O_4 supercapacitor device: (**a**) cycling stability after 10,000 GCD cycles; (**b**) Ragone plot showing the relationship between energy density and power density.

The high similarity between the initial and final GCD profiles shown in Figure 8a suggests that the electrode maintains its structural integrity to a large extent, with no drastic performance degradation during prolonged cycling. However, it should be noted that capacitance retention alone does not provide direct evidence for the complete absence

of structural or chemical changes at the electrode/electrolyte interface. Nevertheless, the observed stability can be attributed to several beneficial complementary factors: (i) the activated carbon (Cm-AC) framework provides structural support for Fe_3O_4 nanoparticles, reducing particle aggregation and mechanical stress during repeated cycling; (ii) the reversible Fe^{2+}/Fe^{3+} redox transitions contribute to stable faradaic charge-storage; and (iii) the stable electrode/electrolyte interface minimizes resistance changes during long-term operation. These factors collectively contribute to reduced capacitance decay and improved cycling durability [8,16,23,43].

The practical applicability of supercapacitor devices depends strongly on achieving an appropriate balance between energy density (Wh kg^{-1}) and power density (W kg^{-1}). The Ragone plot presented in Figure 8b demonstrates the energy–power characteristics of the Cm-AC@Fe_3O_4 symmetric device. The device delivered a maximum energy density of 10.35 Wh kg^{-1} at a power density of 396 W kg^{-1}. Even when the power density increased to 1005 W kg^{-1}, the device maintained an energy density of 1.37 Wh kg^{-1}. These results demonstrate that the incorporation of Fe_3O_4 effectively enhances the energy-storage capability of the activated carbon-based electrode while maintaining acceptable power performance.

The enhanced energy density is mainly attributed to the additional faradaic contribution provided by the Fe_3O_4 phase, which complements the EDLC-based charge-storage of the activated carbon matrix. The decrease in energy density with increasing power density observed in the Ragone plot is typical for supercapacitor systems and can be associated with limited ion diffusion into internal active sites at high current densities, as well as increased voltage losses caused by internal resistance (IR drop). Overall, the Cm-AC@Fe_3O_4 symmetric device exhibits a balanced combination of capacitance retention, energy density, and power capability, confirming the beneficial role of Fe_3O_4 incorporation into biomass-derived activated carbon electrodes for advanced supercapacitor applications.

4. Conclusions

This study demonstrates that the Cm-AC@Fe_3O_4 hybrid material provides enhanced electrochemical performance not only in a three-electrode configuration but also in a practical symmetric supercapacitor device. The assembled Cm-AC@Fe_3O_4//Cm-AC@Fe_3O_4 symmetric device exhibited good long-term stability, maintaining 87.5% of its initial capacitance after 10,000 galvanostatic charge–discharge cycles, indicating the durability of the hybrid electrode structure during prolonged operation. The obtained energy–power characteristics confirm that Fe_3O_4 incorporation effectively improves the charge-storage capability of biomass-derived activated carbon by introducing additional pseudocapacitive contributions while preserving the advantages of the carbon framework.

The enhanced electrochemical behavior of the Cm-AC@Fe_3O_4 electrode was attributed to the beneficial complementary combination of the porous activated carbon matrix and the reversible Fe^{2+}/Fe^{3+} redox activity of Fe_3O_4 nanoparticles. Structural, morphological, and electrochemical analyses, including SEM, EDX, XRD, BET, FTIR, CV, GCD, and EIS measurements, confirmed the successful formation and electrochemical functionality of the hybrid material and its improved charge-transfer properties. The CV and GCD results demonstrated increased specific capacitance, while EIS analysis revealed reduced resistance and improved electrode kinetics after Fe_3O_4 modification.

Furthermore, the biomass-derived synthesis strategy used for the preparation of Cm-AC and Cm-AC@Fe_3O_4 provides a sustainable approach for developing carbon-based hybrid electrode materials for energy storage applications. The obtained results indicate that the Cm-AC@Fe_3O_4 hybrid electrode is a promising candidate for advanced supercapacitor systems requiring a combination of high capacitance, good cycling stability, and improved energy-storage capability. Despite the encouraging electrochemical performance, further

optimization of Fe_3O_4 loading, pore structure, and electrode architecture will be necessary to improve long-term cycling stability and energy density. In addition, while the present study focused primarily on the electrochemical properties, the intrinsic magnetic nature of Fe_3O_4 nanoparticles offers potential for multifunctional applications, such as magnetic separation and magnetically assisted energy storage. Comprehensive magnetic characterization (e.g., VSM analysis) will be pursued in future studies to fully elucidate the magneto-electrochemical properties of this hybrid system. Future studies should also evaluate the material in practical flexible or asymmetric supercapacitor configurations. Future developments involving the integration of battery-type and supercapacitor-type materials may provide additional opportunities for designing hybrid energy storage systems with improved energy density and power capability for applications such as electric vehicles, energy management systems, and portable electronic devices.

Author Contributions: Conceptualization, M.F.B.; methodology, M.F.B. and A.L.; validation, T.K.; formal analysis, A.L.; investigation, M.F.B., V.T., S.E., M.Ö., A.E., A.L., F.Y., T.K., O.Š., B.Z., D.I., R.K. and O.S.; resources, E.K.; data curation, A.E., and T.K.; writing—original draft preparation, M.F.B., V.T., S.E., M.Ö., A.E., A.L. and F.Y.; writing—review and editing, T.K., O.Š., E.K., B.Z., R.K. and O.S.; visualization, O.Š.; supervision, M.F.B. and O.S.; project administration, E.K. All authors have read and agreed to the published version of the manuscript.

Funding: This work was supported in part by the Ministry of Education and Science of Ukraine (projects Nos. 0125U002005 and 0125U002033), National Research Foundation of Ukraine (project No. 2020.02/0100), Slovak Grant Agency VEGA (project No. 2/0131/25), Slovak Research and Development Agency (project No. APVV-21-0335), MSCA4Ukraine (grant No. 1128327), funded by the European Union, US National Science Foundation (NSF) grant CBET-2235349, including IMPRESS-U and REU supplements, and NSF-BSF grant CBET-2422672.

Data Availability Statement: The original contributions presented in this study are included in the article. Further inquiries can be directed to the corresponding authors.

Acknowledgments: T.K. acknowledges SAIA (Slovak Academic Information Agency) for a scholarship at the Institute of Physics of the Slovak Academy of Sciences within the framework of the National Scholarship Program of the Slovak Republic.

Conflicts of Interest: The authors declare no conflicts of interest.

References

1. International Energy Agency (IEA). *Global Energy Review 2025*; IEA: Paris, France, 2025. Available online: https://www.iea.org/reports/global-energy-review-2025 (accessed on 17 September 2026).
2. Suraparaju, S.K.; Samykano, M.; Vennapusa, J.R.; Rajamony, R.K.; Balasubramanian, D.; Said, Z.; Pandey, A.K. Challenges and prospectives of energy storage integration in renewable energy systems for net zero transition. *J. Energy Storage* **2025**, *125*, 116923. [CrossRef]
3. Isidorio, D.; Santos, É.; Filho, A.; da Silveira, P.; Eltom, A.; de Biasi, R. Use of cobalt ferrite and activated carbon in supercapacitors. *Process. Appl. Ceram.* **2023**, *17*, 14–22. [CrossRef]
4. Chaiammart, N.; Vignesh, V.; Thu, M.M.; Eiad-ua, A.; Maiyalagan, T.; Panomsuwan, G. Chemically activated carbons derived from cashew nut shells as potential electrode materials for electrochemical supercapacitors. *Carbon Resour. Convers.* **2024**, *8*, 100267. [CrossRef]
5. Butnoi, P.; Pangon, A.; Berger, R.; Butt, H.-J.; Intasanta, V. Electrospun nanocomposite fibers from lignin and iron oxide as supercapacitor material. *J. Mater. Res. Technol.* **2021**, *12*, 2153–2167. [CrossRef]
6. Palem, R.R.; Ramesh, S.; Yadav, H.M.; Kim, J.H.; Sivasamy, A.; Kim, H.S.; Kim, J.-H.; Lee, S.-H.; Kang, T.J. Nanostructured Fe_2O_3@nitrogen-doped multiwalled nanotube/cellulose nanocrystal composite material electrodes for high-performance supercapacitor applications. *J. Mater. Res. Technol.* **2020**, *9*, 7615–7627. [CrossRef]
7. Baran, M.F.; Huseynov, E.; Eftekhari, A.; Levent, A.; Ertaş, E.; Kavetskyy, T.; Šauša, O.; Katz, E.; Smutok, O. High-capacitance gold nanoparticles from *Rhus coriaria*: Green synthesis, characterization and electrochemical evaluation for supercapacitor technologies. *Micromachines* **2026**, *17*, 82. [CrossRef] [PubMed]

8. Aslan, K.S.; Ertaş, E.; Baran, M.F.; Levent, A.; Tümür, Ş.; Eftekhari, A.; Šauša, O.; Smutok, O.; Kavetskyy, T.; Katz, E. Enhanced electrochemical performance of supercapacitors using Fe_3O_4-doped biomass-derived activated carbon electrodes. *Electrochem. Sci. Adv.* **2026**, *6*, e70014. [CrossRef]
9. Ge, K.; Shao, H.; Lin, Z.; Taberna, P.-L.; Simon, P. Advanced characterization of confined electrochemical interfaces in electrochemical capacitors. *Nat. Nanotechnol.* **2025**, *20*, 196–208. [CrossRef] [PubMed]
10. Hasanova, G.; Omarova, S.; Abdullayeva, N.; Khalilov, R.; Mammadova, A.; Baran, M.F.; Levent, A.; Adican, M.T.; Eftekhari, A.; Kavetskyy, T.; et al. Bioinspired silver nanoparticles from *Artemisia lerchiana* as durable electrodes for next-generation supercapacitors. *Phys. Chem. Chem. Phys.* **2026**, *28*, 8706–8714. [CrossRef] [PubMed]
11. Ahmed, S.; Ahmed, A.; Rafat, M. Supercapacitor performance of activated carbon derived from rotten carrot in aqueous, organic and ionic liquid based electrolytes. *J. Saudi Chem. Soc.* **2018**, *22*, 993–1002. [CrossRef]
12. Soam, A.; Kumar, R.; Thatoi, D.; Singh, M. Electrochemical performance and working voltage optimization of nickel ferrite/graphene composite based supercapacitor. *J. Inorg. Organomet. Polym. Mater.* **2020**, *30*, 3325–3331. [CrossRef]
13. Gerard, O.; Numan, A.; Krishnan, S.; Khalid, M.; Subramaniam, R.; Kasi, R. A review on the recent advances in binder-free electrodes for electrochemical energy storage application. *J. Energy Storage* **2022**, *50*, 104283. [CrossRef]
14. Hamid, M.; Haida Mohd Kaus, N.; Humaidi, S.; Isnaeni, I.; Daulay, A.; Revita Saragi, I. Activated carbon from biomass waste candlenut shells (Aleurites moluccana) doped ZIF-67/Fe_3O_4 as advanced materials for supercapacitor. *Mater. Sci. Energy Technol.* **2024**, *7*, 381–390. [CrossRef]
15. Solmaz, A.; Turna, T.; Baran, A. Green synthesis of Fe_3O_4-*Crataegus tanacetifolia* (Lam.) biochar magnetic nanocomposites for adsorption of naproxen. *Chem. Eng. Technol.* **2025**, *48*, e70019. [CrossRef]
16. He, P.; Yang, K.; Wang, W.; Dong, F.; Du, L.; Liu, H. Nanosized Fe_3O_4-modified activated carbon for supercapacitor electrodes. *Russ. J. Electrochem.* **2013**, *49*, 354–358. [CrossRef]
17. Jayakumar, S.; Santhosh, P.C.; Mohideen, M.M.; Radhamani, A.V. A comprehensive review of metal oxides (RuO_2, Co_3O_4, MnO_2 and NiO) for supercapacitor applications and global market trends. *J. Alloys Compd.* **2024**, *976*, 173170. [CrossRef]
18. Weerasuk, B.; Chutimasakul, T.; Prigyai, N.; Nilgumhang, K.; Kaeopookum, P.; Sangtawesin, T. Structural and electrochemical evolution of water hyacinth-derived activated carbon with gamma pretreatment for supercapacitor applications. *Materials* **2024**, *17*, 3233. [CrossRef] [PubMed]
19. Adli, R.G.; Su, Y.; Hosseini, M.G.; Hajalilou, A. Metal oxides for supercapacitors. In *Handbook of Supercapacitor Materials*; Wiley: Hoboken, NJ, USA, 2021; pp. 245–283. [CrossRef]
20. Lakra, R.; Kumar, R.; Kumar Sahoo, P.; Kumar, S.; Soam, A. Application of iron oxide in supercapacitor. In *Iron Oxide Nanoparticles*; IntechOpen: London, UK, 2022. [CrossRef]
21. Güneş, M.; Ertaş, E.; Tumur, S.; Zulfugarova, P.; Nuriyeva, F.; Kavetskyy, T.; Kukhazh, Y.; Grozdov, P.; Šauša, O.; Smutok, O.; et al. Synthesis and antibacterial evaluation of silver-coated magnetic iron oxide/activated carbon nanoparticles derived from *Hibiscus esculentus*. *Magnetochemistry* **2025**, *11*, 53. [CrossRef]
22. Chen, C.-C.; Chen, C.-Y.; Tsay, C.-Y.; Wang, S.-Y.; Lin, C.-K. Influence of Fe_3O_4 nanoparticles on pseudocapacitive behavior of the charge storage process. *J. Alloys Compd.* **2015**, *645*, 250–258. [CrossRef]
23. Guan, C.; Liu, J.; Wang, Y.; Mao, L.; Fan, Z.; Shen, Z.; Zhang, H.; Wang, J. Iron oxide-decorated carbon for supercapacitor anodes with ultrahigh energy density and outstanding cycling stability. *ACS Nano* **2015**, *9*, 5198–5207. [CrossRef] [PubMed]
24. Liu, M.; Ye, Y.; Ye, J.; Gao, T.; Wang, D.; Chen, G.; Song, Z. Recent advances of magnetite (Fe_3O_4)-based magnetic materials in catalytic applications. *Magnetochemistry* **2023**, *9*, 110. [CrossRef]
25. Serga, V.; Burve, R.; Maiorov, M.; Krumina, A.; Skaudžius, R.; Zarkov, A.; Kareiva, A.; Popov, A.I. Impact of gadolinium on the structure and magnetic properties of nanocrystalline powders of iron oxides produced by the extraction-pyrolytic method. *Materials* **2020**, *13*, 4147. [CrossRef] [PubMed]
26. Khandaker, T.; Islam, T.; Nandi, A.; Anik, M.A.A.M.; Hossain, M.S.; Hasan, M.K.; Hossain, M.S. Biomass-derived carbon materials for sustainable energy applications: A comprehensive review. *Sustain. Energy Fuels* **2025**, *9*, 693–723. [CrossRef]
27. Park, S.; Raj, C.J.; Manikandan, R.; Kim, B.C.; Yu, K.H. Improved electrochemical performance of Fe_3O_4 nanoparticles decorated activated carbon supercapacitor electrodes. *Bull. Korean Chem. Soc.* **2020**, *41*, 856–863. [CrossRef]
28. Pires, B.M.; Nunes, W.G.; Freitas, B.G.; Oliveira, F.E.R.; Katic, V.; Rodella, C.B.; Da Silva, L.M.; Zanin, H. Characterization of porous cobalt hexacyanoferrate and activated carbon electrodes under dynamic polarization conditions in a sodium-ion pseudocapacitor. *J. Energy Chem.* **2021**, *54*, 53–62. [CrossRef]
29. Teo, E.Y.L.; Muniandy, L.; Ng, E.-P.; Adam, F.; Mohamed, A.R.; Jose, R.; Chong, K.F. High surface area activated carbon from rice husk as a high performance supercapacitor electrode. *Electrochim. Acta* **2016**, *192*, 110–119. [CrossRef]
30. Ertaş, E.; Doğan, S.; Baran, A.; Baran, M.F.; Evcil, M.; Kurt, B.; Güneş, Z.; Aslan, K.S. Preparation and characterization of silver-loaded magnetic activated carbon produced from *Crataegus monogyna* for antimicrobial and antioxidant applications. *ChemistrySelect* **2025**, *10*, e202405558. [CrossRef]

31. Baran, A.; Ertaş, E. Preparation, characterization and in vitro applications of morin hydrate loaded HPAC@MNPs nanocomposite. *Iğdır Üniv. Bilim. Enst. Derg.* **2025**, *15*, 217–227. [CrossRef]
32. Baran, A.; Ertaş, E.; Baran, M.F.; Eftekhari, A.; Gunes, Z.; Keskin, C.; Usanov, S.A.; Khalilov, R. Green-synthesized characterization, antioxidant and antibacterial applications of CtAC/MNPs-Ag nanocomposites. *Pharmaceuticals* **2024**, *17*, 772. [CrossRef] [PubMed]
33. Kępińska-Pacelik, J.; Biel, W. Hawthorn (*Crataegus monogyna* Jacq.): A review of therapeutic potential and applications. *Molecules* **2026**, *31*, 226. [CrossRef] [PubMed]
34. Colares, C.J.G.; Pastore, T.C.M.; Coradin, V.T.R.; Camargos, J.A.A.; Moreira, A.C.O.; Rubim, J.C.; Braga, J.W.B. Exploratory analysis of the distribution of lignin and cellulose in woods by Raman imaging and chemometrics. *J. Braz. Chem. Soc.* **2015**, *26*, 1297–1305. [CrossRef]
35. Nabavi, S.F.; Habtemariam, S.; Ahmed, T.; Sureda, A.; Daglia, M.; Sobarzo-Sánchez, E.; Nabavi, S.M. Polyphenolic composition of *Crataegus monogyna* Jacq.: From chemistry to medical applications. *Nutrients* **2015**, *7*, 7708–7728. [CrossRef] [PubMed]
36. Pandhare, A.B.; Mulik, S.V.; Keshta, B.E.; Nikam, P.N.; Ayyar, M.; Santhoshkumar, S.; Rajendran, S.; Koheil, H.; Kadam, M.R.; Alotibi, A.A.; et al. Energy storage studies of a novel green route synthesized high-performance supercapacitor based on Fe_3O_4. *J. Mater. Sci. Mater. Electron.* **2026**, *37*, 21. [CrossRef]
37. Pandhare, A.B.; Mulik, S.V.; Nikam, P.N.; Phalake, S.S.; Khot, V.M.; Ayyar, M.; Ramasamy, S.; Delekar, S.D.; Patil, R.P.; Prabhu, P.; et al. Titano-magnetite nanoparticles for supercapacitors and magnetic hyperthermia performance. *Sci. Rep.* **2025**, *15*, 23505. [CrossRef] [PubMed]
38. Thommes, M.; Kaneko, K.; Neimark, A.V.; Olivier, J.P.; Rodriguez-Reinoso, F.; Rouquerol, J.; Sing, K.S.W. Physisorption of gases, with special reference to the evaluation of surface area and pore size distribution (IUPAC technical report). *Pure Appl. Chem.* **2015**, *87*, 1051–1069. [CrossRef]
39. Vashchynskyi, V. Porous carbon materials derived from apricot pits for electrical energy storage devices and sorption technologies: A review of the precursors, preparation methods, and applications. *Fuller. Nanotub. Carbon Nanostruct.* **2026**, *34*, 88–101. [CrossRef]
40. Saka, C.; Levent, A. Robust and highly mesoporous magnesium oxide and nitrogen atoms incorporated hierarchical porous carbon particles as electrode material for high-performance energy storage in acidic, neutral, and basic electrolytes. *Environ. Sci. Pollut. Res.* **2025**, *32*, 20103–20115. [CrossRef] [PubMed]
41. Saha, P.; Islam, M.Z.; Shah, S.S.; Shaikh, M.N.; Maiyalagan, T.; Aziz, M.A.; Ahammad, A.J.S. Harnessing the power of marine biomass-derived carbon for electrochemical energy storage. *Battery Energy* **2025**, *4*, e20240055. [CrossRef]
42. Shah, S.S. Biomass-derived carbon materials for advanced metal-ion hybrid supercapacitors: A step towards more sustainable energy. *Batteries* **2024**, *10*, 168. [CrossRef]
43. Rahaman, M.; Mukherjee, T.; Kaparaju, P.; Bose, S. Iron oxide- and copper oxide-decorated chemically reduced graphene oxide composite as a novel electrode for hybrid supercapacitors. *Energy Fuels* **2022**, *36*, 3976–3986. [CrossRef]
44. Lu, S.; Fang, L.; Wang, X.; Liu, T.X.; Zhao, X.; Bin Xu, B.; Hua, Q.; Liu, H. Insights into activators on biomass-derived carbon-based composites for electrochemical energy storage. *Mater. Today Chem.* **2024**, *37*, 101988. [CrossRef]
45. Wang, J.; Polleux, J.; Lim, J.; Dunn, B. Pseudocapacitive contributions to electrochemical energy storage in TiO_2 (anatase) nanoparticles. *J. Phys. Chem. C* **2007**, *111*, 14925–14931. [CrossRef]
46. Augustyn, V.; Simon, P.; Dunn, B. Pseudocapacitive oxide materials for high-rate electrochemical energy storage. *Energy Environ. Sci.* **2014**, *7*, 1597–1614. [CrossRef]
47. Harish, S.; Sathyakam, P.U. Dunn's method for distinguishing charge storage mechanisms in supercapacitors: A Status Quo Review. *J. Electron. Mater.* **2025**, *54*, 10858–10872. [CrossRef]
48. Zang, X.; Shen, C.; Sanghadasa, M.; Lin, L. High-voltage supercapacitors based on aqueous electrolytes. *ChemElectroChem* **2019**, *6*, 976–988. [CrossRef]
49. Barzegar, F.; Momodu, D.Y.; Fashedemi, O.O.; Bello, A.; Dangbegnon, J.K.; Manyala, N. Investigation of different aqueous electrolytes on the electrochemical performance of activated carbon-based supercapacitors. *RSC Adv.* **2015**, *5*, 107482–107487. [CrossRef]

Disclaimer/Publisher's Note: The statements, opinions and data contained in all publications are solely those of the individual author(s) and contributor(s) and not of MDPI and/or the editor(s). MDPI and/or the editor(s) disclaim responsibility for any injury to people or property resulting from any ideas, methods, instructions or products referred to in the content.